Exploring the dynamic characteristics of thermoelectric generator under fluctuations of exhaust heat

Ding Luo[a,b], Yuying Yan[c], Wei-Hsin Chen[d,e,f], Bingyang Cao[a,*]

[a] Key Laboratory for Thermal Science and Power Engineering of Ministry of Education, Department of Engineering Mechanics, Tsinghua University, Beijing 100084

[b] College of Electrical Engineering & New Energy, China Three Gorges University, Yichang 443000, China

[c] Faculty of Engineering, University of Nottingham, University Park, Nottingham NG7 2RD, UK

[d] Department of Aeronautics and Astronautics, National Cheng Kung University, Tainan 701, Taiwan

[e] Research Center for Smart Sustainable Circular Economy, Tunghai University, Taichung 407, Taiwan

[f] Department of Mechanical Engineering, National Chin-Yi University of Technology, Taichung 411, Taiwan

Corresponding authors: caoby@tsinghua.edu.cn

Abstract: The thermoelectric generator is a potential candidate to recover waste heat from exhaust gas. Regarding the fluctuations of exhaust heat in practical situations, this paper adopts a transient fluid-thermal-electric multiphysics model to investigate the dynamic performance of the thermoelectric generator. Results show that the fluctuation of exhaust temperature has a greater influence on the dynamic characteristics than the fluctuation of exhaust mass flow rate. The dynamic performance of the thermoelectric generator benefits from a decrease in exhaust heat, but suffers when the exhaust heat is in an upward trend. Compared with the constant power and efficiency values of 4.96 W and 2.49%, the average power and efficiency of the thermoelectric generator show a notable increase of 5.50% and 70.61% respectively during a step decrease in exhaust mass flow rate. Similarly, under a linear decrease, the mean power and efficiency experience a rise of 6.04% and 45.05% respectively. Besides, periodic exhaust heat can effectively amplify the dynamic output performance, especially for conversion efficiency. When subjected to a sin wave of exhaust mass flow rate, the efficiency experiences a 15.58% improvement. This work offers a comprehensive understanding of the dynamic characteristics exhibited by the thermoelectric generator employed for waste heat recovery.

Keywords: thermoelectric generator; dynamic characteristics; waste heat recovery; exhaust heat.

Nomenclature

Greek symbols		R	load resistance, Ω
ρ	density, kg·m^{-3}	S	Seebeck coefficient, μV·K^{-1}
λ	thermal conductivity, W·m^{-1}·K^{-1}	t	time, s
η	conversion efficiency	T	temperature, K
σ^{-1}	electrical resistivity, Ω·m	U	output voltage, V
φ	electric potential, V	$\vec{v}$	Velocity, m·s^{-1}
μ	dynamic viscosity, Pa·s	*Abbreviations*	
ε	turbulent dissipation rate, m^2·s^{-3}	CFD	computational fluid dynamics
Symbols		TEG	thermoelectric generator
c	specific heat capacity, J·kg^{-1}·K^{-1}	TEM	thermoelectric module
$\vec{E}$	electric field density vector, V·m^{-2}	*Subscripts*	
$\vec{J}$	current density vector, A·m^{-2}	co	copper electrodes
k	turbulent kinetic energy, m^2·s^{-2}	ex	exhaust heat
$\dot{m}$	mass flow rate, g·s^{-1}	h	hot side
P	output power, W	L	load resistance
p	pressure, Pa	m	material name
Q	heat absorption, W	n	n-type thermoelectric semiconductors
		out	exhaust outlet
		p	p-type thermoelectric semiconductors

1. Introduction

In the areas of industrial production and engines, the exhaust gas generated carries a considerable amount of heat, which can be converted into electrical energy or useful thermal energy through waste heat recovery technologies, thereby reducing energy consumption and pollution. Turbo-charging [1], Rankine cycle [2], heat pump [3], and thermoelectric generator (TEG) [4-6] are the commonly used waste heat recovery technologies. Among these, the TEG, as a solid heat-to-electricity energy converter, has received great attention in the field of waste heat recovery, because of its unparalleled merits of no moving parts, no emissions, and long service life [7]. With the progress of high-performance thermoelectric materials, there is a rising trend among researchers to utilize thermoelectric generators (TEGs) for the recovery of waste heat.

In the context of industrial waste heat recovery, Meng et al. [8] employed computational fluid dynamics (CFD) tools to examine the performance of the thermoelectric generator (TEG) and optimize the structural parameters of both the TEG and heat collector; They recommended using a heat collector with 19 fins, each with a height of 8 cm, and an overall TEG size of 20 cm × 150 cm. Wang et al. [9] integrated heat pipes into the TEG to effectively harvest heat from industrial exhaust, and verified the feasibility of TEG applications in industrial waste heat recovery through experiments. In the scenario of ship waste heat recovery, Eddine et al. [10] studied and compared the output performance of two TEGs based on Bi_2Te_3 and $Si_{80}Ge_{20}$ thermoelectric materials for a marine diesel engine; They found that the Bi_2Te_3-based TEG outperforms the $Si_{80}Ge_{20}$-based one, and the power output of the TEG using Bi_2Te_3 thermoelectric materials can reach 982 W/m^2 at the engine speed of 1000 rpm, while using $Si_{80}Ge_{20}$ thermoelectric materials can only achieve 756 W/m^2. Chariklia et al. [11] proposed a modular dynamic mathematical model of the TEG to evaluate its potential for waste heat recovery from a seagoing vessel; The simulation results indicated that the TEG could generate 26 kW of electricity when applied to a very large crude oil carrier and 1 kW when applied to an auxiliary engine. The TEG has witnessed good application prospects in industrial and ship waste heat recovery. Another promising application of TEGs is to harvest waste heat from automobile exhaust. Quan et al. [12] studied the performance interaction relationship between the TEG and automobile engine through CFD simulations; They revealed that the inner topology and engine operating condition significantly affect the behavior of the TEG, and TEGs offer the dual benefits of improving fuel economy and reducing emissions. Lan et al. [13] conducted a comparison of the output performance of the TEG when applied to extended-range electric vehicles and traditional vehicles; Through theoretical analysis, they found that the auxiliary power and driving cycle only affect the performance of the TEG in conventional vehicles, with little impact on its performance in extended-range electric vehicles. Recent advancements in TEG technology have led to the emergence of numerous prototypes specifically designed for automobile waste heat recovery [14-16].

A reasonable model is the basis for performance analysis and optimization of the TEG. To ensure an accurate assessment of its performance, a plethora of theoretical models, such as CFD models [17], analytical models [18], and multiphysics numerical models [19], have been developed. For the TEG placed between a high-temperature wastewater channel and a low-temperature air channel, Chen et al. [20] presented a performance prediction method based on CFD simulations; The prediction results indicated that the TEG could reach the highest power and efficiency of 0.411 W and 0.95% while using 27 fins in the air channel, which are respectively 105.5% and 43.94% higher than those of the TEG without fins. Zhao et al. [21] developed a new automobile TEG with a perforated plate and analyzed its performance through the coupling simulations of the thermal-electric numerical model and CFD model; Also, the authors carried out an optimization study on the placement of the perforated plate and discovered that the optimized automobile TEG achieved a 73.4% higher output power compared to the TEG without a perforated plate. Considering the fast calculating speed and convenience of the analytical model, Cai et al. [22] offered a sizing optimization approach for the structural parameters of the thermoelectric module (TEM) and heat exchanger, in which the output performance is computed by an analytical model; Their results suggested that the optimal number and height of the TEM are 144 and 1.5 mm respectively. Based on a thermal resistance network, Catalan et al. [23] developed an analytical model to assess the performance of TEGs applied to recover geothermal energy and pointed out that the TEG could generate 681.53 MWh of electricity per year. However, the CFD model and analytical model may lead to unreasonable prediction results due the neglect of multiphysics field coupling mechanism. Therefore, multiphysics numerical models have emerged in recent studies [24, 25]. Yan et al. [26] proposed a modular TEG design with heat pipes for the purpose of waste heat recovery from passenger vehicles, and developed a comprehensive fluid-thermal-electric multiphysics model to assess its operational characteristics; The research outcomes demonstrated the advantageous effect of heat pipes on improving the heat transfer efficiency of the TEGs, allowing for a maximum output power of 29.8 W per unit. In a previous study, Luo et al. [27] provided an overview of the advancements in theoretical modeling of the TEG, encompassing various aspects such as TEG units to TEG systems, one-dimensional to three-dimensional models, and steady-state to transient-state analysis.

Given the dynamic nature of exhaust heat in real-world scenarios, transient performance analysis of the TEG offers a more accurate reflection of the practical conditions in comparison to steady-state analysis. Massaguer et al. [28] explored the dynamic characteristics of the automotive TEG under the New European Driving Cycle using CFD simulations and experimental tests, revealing that the output power of the TEG observed during transient experiments is smaller than the predictions from steady-state numerical simulations. Lan et al. [29] expanded the existing analytical model from steady state to transient state and applied it to study the dynamic behavior of the automotive TEG throughout an entire driving cycle; The developed model allowed for the calculation of the dynamic temperatures and output power of the TEG. Moreover, Luo et al. [30] presented a new transient dynamic model that combines the CFD model and the analytical model, taking advantage of the analytical model's computational efficiency and the CFD model's accuracy improvement potential. So far, several transient models have been formulated for TEGs employed in the recuperation of waste heat. Nevertheless, existing research primarily focuses on the transient performance analysis of TEGs under specific operating conditions, with no mention of the impact of exhaust heat parameters on their dynamic performance. In Ref. [31], it has been proved that periodic heating is conducive to amplify the output performance of the TEM. For the application of exhaust waste heat recovery, the exhaust heat in actual situations exhibits irregular fluctuations, and the periodic exhaust heat may also be helpful to enhance the behavior of the TEG. Therefore, examining the dynamic characteristics of the TEG in the presence of exhaust heat fluctuations is vital for a comprehensive understanding and effective utilization of its capabilities.

In contrast to the dynamic behavior of the TEM, the dynamic characteristics of the TEG in waste heat recovery are primarily influenced by fluctuations in exhaust heat, such as exhaust temperature and mass flow rate, rather than the hot-side temperature. To reveal the dynamic characteristics of the TEG under fluctuations of exhaust heat, a simplified TEG is used as the research objective in present study, and a transient fluid-thermal-electric multiphysics model is built to examine its transient output power and conversion efficiency. Besides, six basic waveforms of exhaust heat are selected as boundary conditions for the multiphysics model to explore the optimal transient exhaust heat source, including increases in step and linear, decreases in step and linear, as well as triangular and sine waves.

2. Architecture of the simplified thermoelectric generator

Considering the substantial computational resources necessary for multiphysics numerical simulation and the fact that the dynamic characteristics of the TEG are not reliant on its structure, a simplified TEG arrangement, as shown in Fig. 1, is employed as the research objective. The heat exchanger is equipped with inlet and outlet connectors, each with a diameter of 40 mm, through which the exhaust gas enters and exits. To efficiently capture heat from the exhaust gas, 16 fins are evenly distributed on the two hot sides of the heat exchanger. A TEG1-12708 TEM (Sagreon, Wuhan, China) based on Bi_2Te_3 materials is affixed to one hot side of the heat exchanger, consisting of 127 pairs of p- and n-type thermoelectric semiconductors, 256 copper slices, and two ceramic plates. The TEM exhibits a sandwich structure, where the thermoelectric semiconductors are electrically connected in series and thermally connected in parallel. Dimensions (length × width × height) for the ceramic plate, copper slice, and thermoelectric semiconductor are $40 \times 40 \times 0.7$ mm^3, $1.4 \times 3.8 \times 0.4$ mm^3, and $1.4 \times 1.4 \times 1.6$ mm^3, respectively. The cold side of the TEM is equipped with a heat sink featuring a U-shaped water channel (with a diameter of 5.5 mm), which functions as a cooling source. The overall size of the heat sink is $40 \times 40 \times 12$ mm^3. Driven by the temperature difference between the heat exchanger and heat sink, the TEM will generate electricity, and its output performance depends on the exhaust heat. Fig. 1 provides more detailed structural information for each component mentioned. In addition, Table 1 presents comprehensive material parameters for the TEG, including specific thermoelectric properties supplied by the manufacturer. For the exhaust gas and coolant, the material parameters of dry air and water are adopted to represent their respective material properties.

Table 1. Material characteristics of the TEG

Component	Material name	Density ($kg\cdot m^{-3}$)	Specific heat ($J\cdot kg^{-1}\cdot K^{-1}$)	Thermal conductivity ($W\cdot m^{-1}\cdot K^{-1}$)	Seebeck coefficient ($\mu V\cdot K^{-1}$)	Electrical resistivity ($10^{-5}\Omega\cdot m$)
inlet and outlet connector	stainless steel	8030	502.48	17	-	-
heat exchanger and heat sink	aluminum	2719	871	217.7	-	-
p-type thermoelectric semiconductor	p-type Bi_2Te_3 materials	6780	$1.7289\times10^{-5}T^3-0.0209T^2+8.4401T-945.6858$	$1.6848\times10^{-7}T^3-1.8949\times10^{-4}T^2+0.0697T-6.8387$	$1.3222\times10^{-5}T^3-0.0171T^2+7.3095T-853.6610$	$-9.0350\times10^{-9}T^3+1.6380\times10^{-5}T^2-0.00425T+0.6648$
n-type thermoelectric semiconductor	n-type Bi_2Te_3 materials	7800	$1.0197\times10^{-5}T^3-0.0128T^2+5.3717T-581.5998$	$1.4735\times10^{-7}T^3-1.5903\times10^{-4}T^2+0.0571T-5.0958$	$-1.5235\times10^{-5}T^3+0.0194T^2-8.2297T+981.1090$	$4.4520\times10^{-8}T^3-5.5288\times10^{-5}T^2+0.02591T-3.4085$
copper slice	copper	8960	385	400	-	1.67×10^3
ceramic plate	ceramic	3600	850	$-0.02857T+28.3757$	-	-

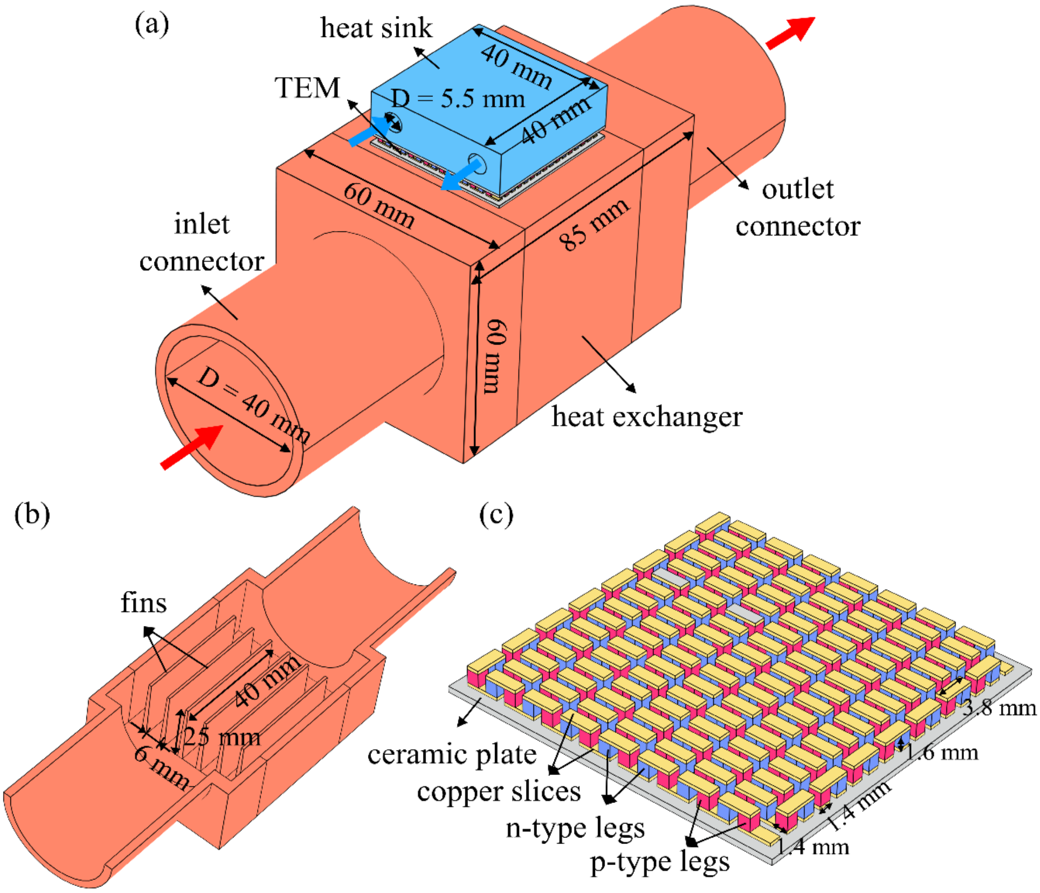

Fig. 1. Architecture of the simplified TEG [32].

3. Model development

The developed model is based on the following assumptions:

(i) The heat radiation is not considered;

(ii) Thermoelectric materials are isotropic;

(iii) The gravity is ignored.

3.1 Basic principles of the transient fluid-thermal-electric multiphysics model

In waste heat recovery applications, the TEG experiences complex multiphysics coupling phenomena, which include the fluid dynamics of exhaust gas and cooling water, the thermal distribution across the entire structure, and the electrical behavior of thermoelectric semiconductors and copper slices. Consequently, it is necessary to consider multiphysics coupling characteristics in the numerical model to ensure the high accuracy of simulations. The CFD theory and k-ε turbulence model [33] are employed to describe the fluid behavior of exhaust gas and cooling water, and the corresponding governing equations include:

$$\frac{\partial \rho}{\partial t} + \nabla \cdot (\rho \vec{v}) = 0 \tag{1}$$

$$\frac{\partial}{\partial t}(\rho \vec{v}) + \nabla \cdot (\rho \vec{v} \vec{v}) = -\nabla p + \nabla \cdot (\mu \nabla \vec{v}) \tag{2}$$

$$\rho c \frac{\partial T}{\partial t} + \rho c \vec{v} \cdot \nabla T = \nabla \cdot (\lambda \nabla T) \tag{3}$$

$$\frac{\partial}{\partial t}(\rho k) + \rho(\vec{v} \cdot \nabla) k = \nabla \cdot \left[\left(\mu + \frac{\mu_t}{\sigma_k}\right) \nabla k\right] + P_k - \rho \varepsilon \tag{4}$$

$$\frac{\partial}{\partial t}(\rho \varepsilon) + \rho(\vec{v} \cdot \nabla) \varepsilon = \nabla \cdot \left[\left(\mu + \frac{\mu_t}{\sigma_\varepsilon}\right) \nabla \varepsilon\right] + C_{1\varepsilon} \frac{\varepsilon}{k} P_k - C_{2\varepsilon} \rho \frac{\varepsilon^2}{k} \tag{5}$$

with

$$\mu_t = \rho C_\mu \frac{k^2}{\varepsilon} \tag{6}$$

where, t, ρ, c, $\vec{v}$, p, λ, μ, and T represent time, density, specific heat, velocity vector, pressure, thermal conductivity, dynamic viscosity, and temperature, respectively. k and ε are respectively the turbulent kinetic energy and its dissipation rate. P_k represents the shear term of k. $C_{1\varepsilon} = 1.44$, $C_{2\varepsilon} = 1.92$, $C_\mu = 0.99$, $\sigma_k = 1.0$, and $\sigma_\varepsilon = 1.3$ are constants.

For components without involving current flow, the thermal field can be described by the energy conservation equation:

$$(\rho c)_{\mathrm{m}} \frac{\partial T}{\partial t} = \nabla \cdot (\lambda_{\mathrm{m}} \nabla T) \tag{7}$$

where, subscript m denotes the name of different materials.

The energy conservation equations governing the thermal field in p- and n-type thermoelectric semiconductors can be mathematically represented as follows [34]:

$$(\rho c)_{\mathrm{p}} \frac{\partial T}{\partial t} = \nabla \cdot \left(\lambda_{\mathrm{p}}(T) \nabla T\right) + \sigma_{\mathrm{p}}^{-1}(T) \vec{J}^2 - T_{\mathrm{p}} \vec{J} \cdot \nabla S_{\mathrm{p}}(T) - \frac{\partial S_{\mathrm{p}}(T)}{\partial T_{\mathrm{p}}} T_{\mathrm{p}} \vec{J} \cdot \nabla T \tag{8}$$

$$(\rho c)_{\mathrm{n}} \frac{\partial T}{\partial t} = \nabla \cdot (\lambda_{\mathrm{n}}(T) \nabla T) + \sigma_{\mathrm{n}}^{-1}(T) \vec{J}^2 - T_{\mathrm{n}} \vec{J} \cdot \nabla S_{\mathrm{n}}(T) - \frac{\partial S_{\mathrm{n}}(T)}{\partial T_{\mathrm{n}}} T_{\mathrm{n}} \vec{J} \cdot \nabla T \tag{9}$$

where, S and σ^{-1} are the Seebeck coefficient and electrical resistivity respectively. $\vec{J}$ represents the current density vector across thermoelectric semiconductors and copper slices. The subscripts p and n are employed to identify the p-type and n-type thermoelectric semiconductors, respectively.

Unlike thermoelectric semiconductors, the energy conservation equation for the thermal field of copper slices does not involve the inclusion of terms concerning the Seebeck coefficient, and it can be described as:

$$(\rho c)_{\mathrm{co}}\frac{\partial T}{\partial t} = \nabla\cdot(\lambda_{\mathrm{co}}\nabla T) + \sigma_{\mathrm{co}}^{-1}\vec{J}^2 \tag{10}$$

where, subscript co denotes copper slices.

As for the electric field, it follows [35]:

$$\vec{E} = -\nabla\varphi + S(T)\nabla T \tag{11}$$

$$\vec{J} = \sigma\vec{E} \tag{12}$$

$$\nabla\cdot\vec{J} = 0 \tag{13}$$

where, $\vec{E}$ and φ represent the electric field density vector and electric potential, respectively.

Eqs (1)-(13) form the essential equations of the transient fluid-thermal-electric multiphysics model. To compute these equations, numerical discretization is applied using the finite element method for spatial variables and the backward difference method for the time variable. The numerical calculations are performed using the commercial software, COMSOL.

According to numerical simulation results, the dynamic characteristics of the TEG can be estimated by extracting corresponding data from physical field distributions, including the dynamic power output $P(t)$ and conversion efficiency $\eta(t)$. Here, the dynamic power output is written by:

$$P(t) = \frac{U_{\mathrm{L}}^2(t)}{R_{\mathrm{L}}} \tag{14}$$

Also, the dynamic conversion efficiency equals the ratio of $P(t)$ to the dynamic heat absorption $Q_{\mathrm{h}}(t)$, that is:

$$\eta(t) = \frac{P(t)}{Q_{\mathrm{h}}(t)} = \frac{P(t)}{c_{\mathrm{ex}}\cdot\dot{m}_{\mathrm{ex}}(t)\cdot[T_{\mathrm{ex}}(t)-T_{\mathrm{out}}(t)]} \tag{15}$$

where T_{out} represents the exhaust outlet temperature.

3.2 Boundary conditions

To accurately estimate the TEG's dynamic behavior when subjected to exhaust heat fluctuations, it is essential to establish corresponding transient boundary conditions on the exhaust channel. Here, the transient state exhaust mass flow inlet boundary condition $\dot{m}_{\mathrm{ex}}(t)$ with the transient temperature $T_{\mathrm{ex}}(t)$ is defined on the inlet surface of the exhaust channel, as illustrated in Fig. 2. Fig. 3 illustrates the changes of exhaust temperature and mass flow rate, ranging from 500 K to 600 K and from 10 g/s to 50 g/s, respectively. To explore the dynamic behavior of the TEG and assess its sensitivity to exhaust temperature and mass flow rate fluctuations, two cases are examined. In the first case, the exhaust mass flow rate undergoes fluctuations while the exhaust temperature is held at a steady-state average of 550 K. In the second case, the exhaust temperature experiences variations while the exhaust mass flow rate is maintained at a steady-state average of 30 g/s. For the outlet surface of the exhaust channel, a pressure outlet boundary condition in a steady state is employed. Besides, a steady-state velocity inlet of 10 m/s with a water temperature of $T_{wa} = 300$ K is defined on the inlet surface of the water channel. On the corresponding outlet surface, a pressure outlet boundary condition is applied. At this point, boundary conditions for the fluid domain have been fully defined. On the surfaces of the solid domain exposed to the environment, a natural convection heat transfer boundary condition is specified. The convection heat transfer coefficient and environmental temperature are set to 10 W·m^{-2}·K^{-1} and 300 K, respectively. As for the electric field boundary conditions in the TEM, a grounded boundary and a voltage coupling boundary are respectively defined on its two terminals. Taking into account the influence of impedance matching, a virtual circuit with load resistance is built on the COMSOL platform, and a voltage coupling boundary is utilized to establish the connection between the load resistance and the TEM.

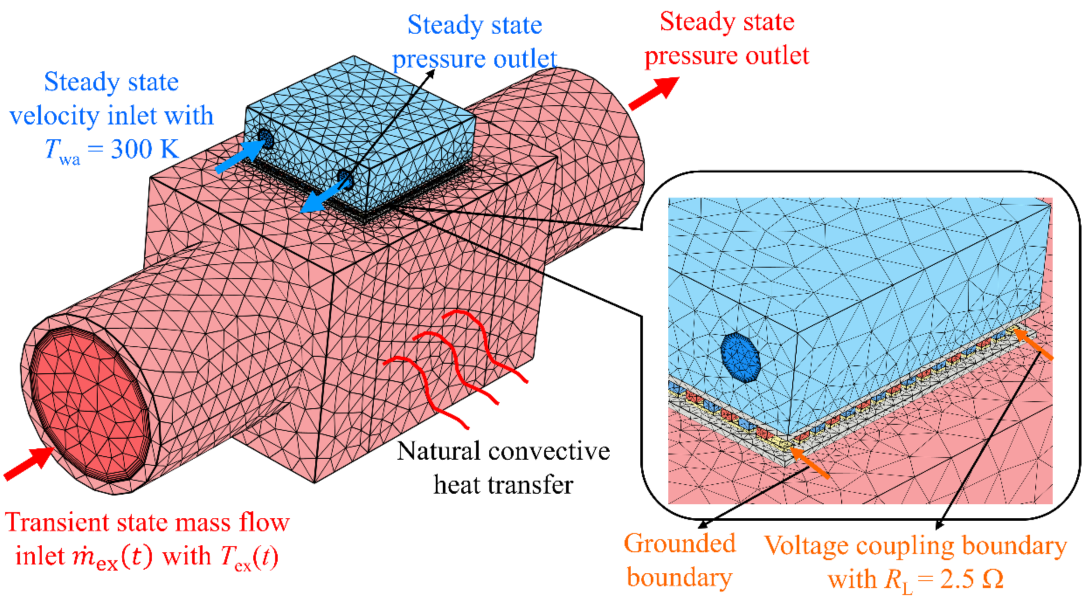

Fig. 2. Schematic diagram of the finite element model and boundary conditions.

Moreover, specific contact resistances are assigned to the corresponding interfaces based on the experiments in Ref. [35]. For instance, contact thermal resistances of 3.65×10^{-5} m^2·K·W^{-1}, 1.78×10^{-4} m^2·K·W^{-1}, and 1.39×10^{-4} m^2·K·W^{-1} are defined on interfaces between copper slices and the ceramic plate, between the TEM and the heat exchanger, and between the TEM and the heat sink, respectively. Similarly, a contact electric resistance of 1.18×10^{-10} Ω·m^2 is introduced on interfaces between copper slices and thermoelectric legs. The incorporation of these contact resistances is essential for ensuring the accuracy of the calculated results.

3.3 Grid independence examination

Due to the sensitivity of finite element simulation results to grid parameters, a grid independence examination is conducted on the finite element model of the TEG to select an appropriate grid system. To ensure the reasonability of numerical calculations, boundary layer grids with 5 layers for the fluid domain and refined grids for the TEM are adopted, as shown in Fig. 2. Four grid systems, namely grid I, II, III, and IV, are selected for the numerical simulations, with respective grid numbers of 691783, 370658, 222694, and 170330. The exhaust mass flow rate, exhaust temperature, and load resistance are set to fixed values of 30 g/s, 550 K, and 2.5 Ω, respectively. The output voltages of the TEG for grid I, II, III, and IV are respectively 3.5217 V, 3.5223 V, 3.5273 V, and 3.5341 V. The more grids there are, the more accurate the numerical results are, but the simulation time also increases accordingly. To ensure accuracy while reducing computation time, grid II is chosen for numerical simulations.

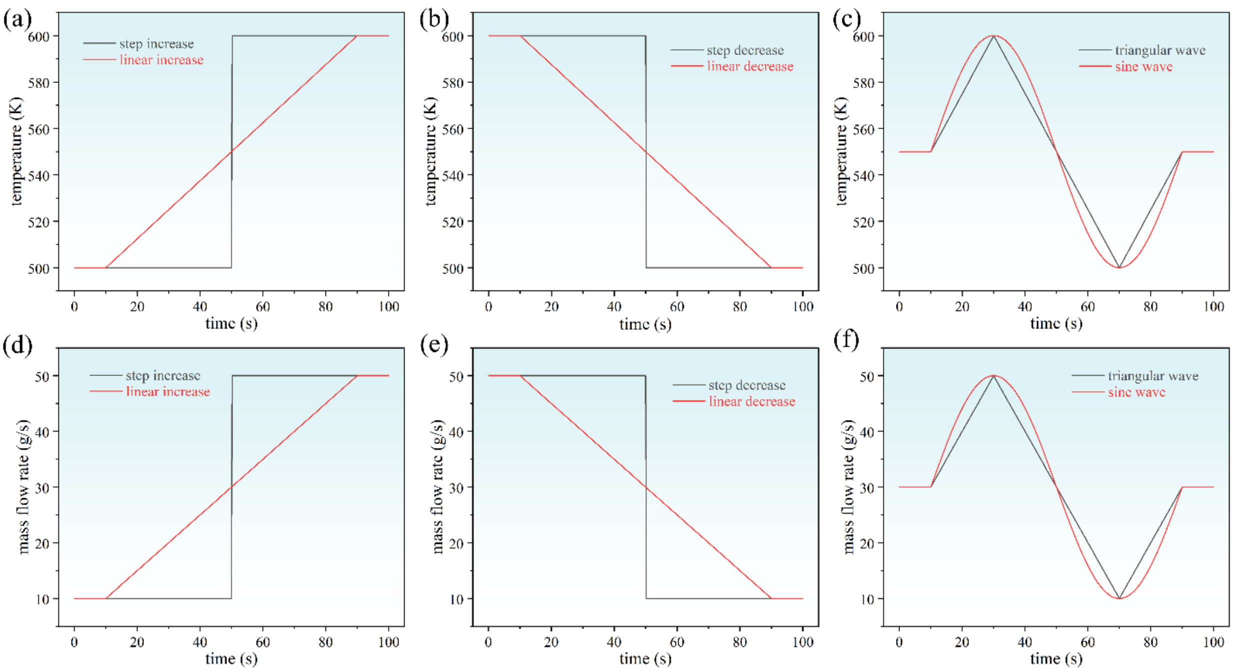

Fig. 3. Fluctuations of the exhaust heat. (a) Step and linear increase of exhaust temperature; (b) Step and linear decrease of exhaust temperature; (c) Triangular and sine wave of exhaust temperature; (d) Step and linear increase of exhaust mass flow rate; (b) Step and linear decrease of exhaust mass flow rate; (c) Triangular and sine wave of exhaust mass flow rate.

3.4 Optimal load resistance

To ensure accurate transient numerical simulations, it is vital to determine the optimal load resistance beforehand. Hence, steady-state numerical simulations are executed on the TEG using Grid II, considering a fixed exhaust mass flow rate of 30 g/s and exhaust temperature of 550 K. The corresponding results are presented in Fig. 4, illustrating the variations in output voltage and power of the TEG for different load resistances. Notably, the output power reaches its peak value when the load resistance is set at 2.5 Ω. Consequently, the optimal load resistance of 2.5 Ω is selected for the subsequent transient numerical simulations in the subsequent sections.

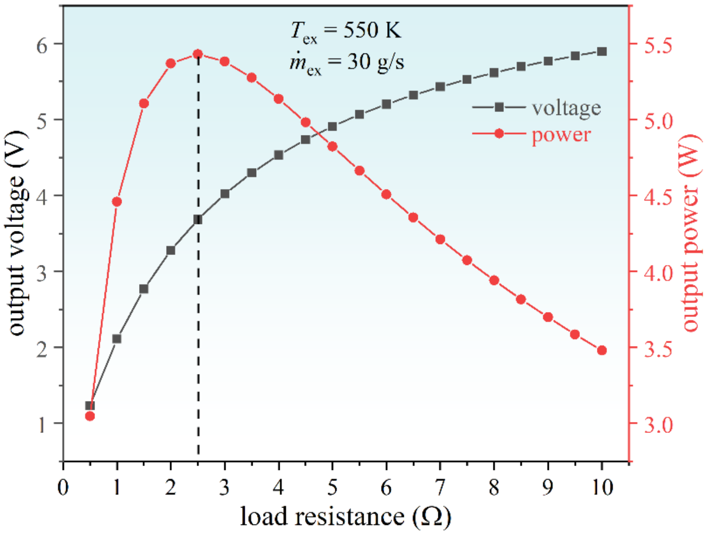

Fig. 4. Exploration of the optimal load resistance.

3.5 Experimental validation

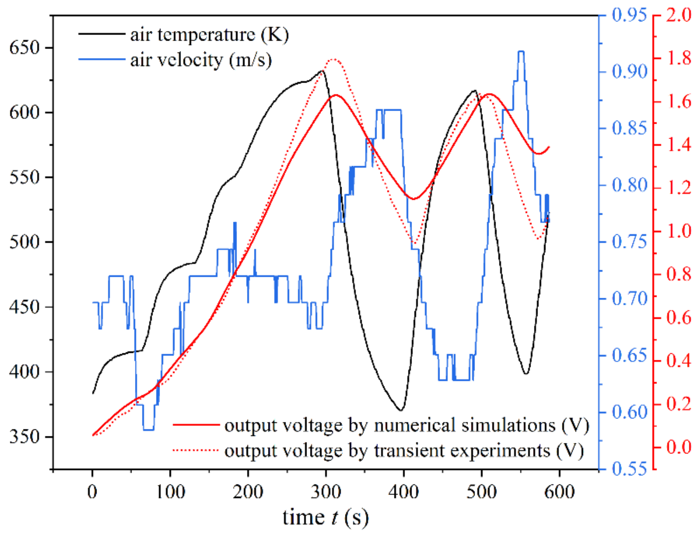

Fig. 5. Model verification by transient experiments [36].

The validity of the transient fluid-thermal-electric multiphysics model has been confirmed through experimental verification in our previous study [36], as depicted in Fig. 5. The transient air temperature and velocity obtained from the experimental tests are employed as the transient boundary conditions for the multiphysics model, and the corresponding simulation results are obtained and compared with the experimental data. Upon comparison, it is observed that the mean error of the output voltage between the experimental and simulation results is approximately 9.24%, which is deemed acceptable for transient experiments, considering the potential measurement errors associated with the instruments.

4. Results and discussion

4.1 Contours of the TEG from numerical simulations

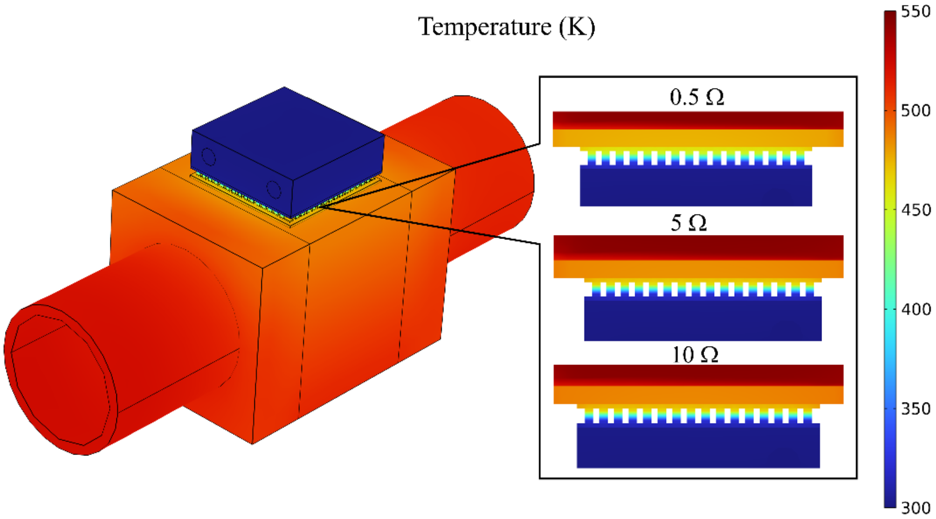

Fig. 6. Temperature contour of the TEG under steady-state conditions of $T_{\mathrm{ex}} = 550$ K and $\dot{m}_{\mathrm{ex}} = 30$ g/s.

Fig. 6 illustrates the temperature contour of the TEG under steady-state conditions of $T_{\mathrm{ex}} = 550$ K and $\dot{m}_{\mathrm{ex}} = 30$ g/s. It is apparent that the temperature difference along the TEM exerts a dominant influence on the temperature reduction between the high-temperature exhaust gas and the low-temperature cooling water, primarily attributable to the limited thermal conduction capabilities of thermoelectric materials. Additionally, the load resistance exerts a notable influence on the temperature distribution on both sides of the TEM. The hot side temperature of the TEM decreases with the decrease in load resistance. This is because the Peltier heat is proportional to the current, and the current increases with the decrease in load resistance. The heat generated by the Peltier effect exhibits heat absorption at the hot side of TEM, resulting in a decrease in temperature and output power. Consequently, the electric field distribution also affects the temperature distribution, and it is more reasonable to predict the behavior of the TEG by taking into account the multiphysics coupling phenomenon.

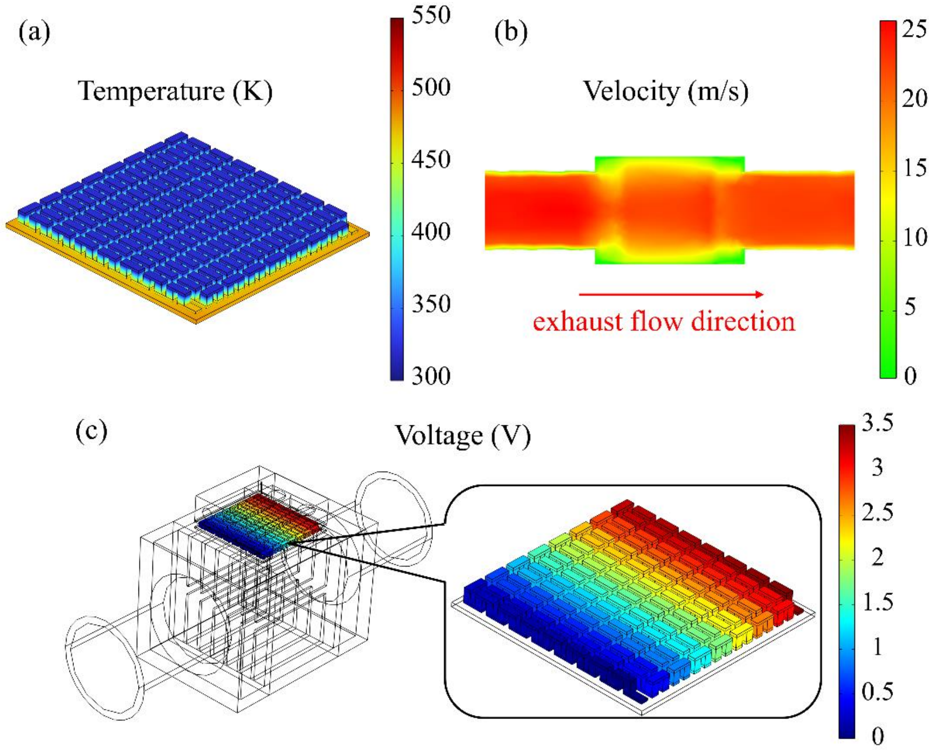

Fig. 7. Other physical field contours of the TEG under steady-state conditions of $T_{\mathrm{ex}} = 550$ K, $\dot{m}_{\mathrm{ex}} = 30$ g/s, and $R_{\mathrm{L}} = 2.5$ Ω. (a) Temperature contour of the TEM; (b) Velocity contour of the exhaust region; (c) Voltage contour of the TEM.

Other physical field contours of the TEG can be found in Fig. 7. As depicted in Fig. 7(a), it is evident that the hot-side temperature of the TEM is markedly lower than the exhaust temperature, while the cold-side temperature closely resembles that of the cooling water. This distinction can be explained by the limited heat capacity of the exhaust gas. Enhancing the heat transfer between the heat exchanger and exhaust gas is one of the effective approaches to improve TEG performance, such as using fin structures. Fig. 7(b) shows the velocity contour in the exhaust channel. Due to the expansion flow from the inlet connector to the heat exchanger, the exhaust velocity located in the heat exchanger is lower than that in connectors, resulting in a lower exhaust temperature. Therefore, how to increase the heat exchanger area for placing TEMs while ensuring sufficient exhaust temperature is also one of the key challenges to be solved in promoting TEG applications. Fig. 7(c) gives the voltage contour of the TEM. The voltage rises proportionally as the number of thermoelectric semiconductors connected in series increases. It is observed that the output voltage is 3.52 V at $R_{\mathrm{L}} = 2.5$ Ω, thus, the corresponding power output is 4.96 W. The fluid-thermal-electric multiphysics model has demonstrated its effectiveness and progressive nature through the simulation results displayed in Figs 6 and 7. To delve further into the dynamic characteristics of the TEG, simulations employing the transient fluid-thermal-electric multiphysics model are performed in the following sections, incorporating fluctuations in exhaust heat as the transient boundary condition. The subsequent analysis of the simulation results sheds light on the dynamic behavior of the TEG.

4.2 Dynamic characteristics under step increase and decrease of the exhaust heat

Fig. 8 illustrates the dynamic power output and exhaust outlet temperature of the TEG under step increase and decrease of the exhaust heat, where the exhaust heat changes at t = 50 s. Although the exhaust heat exhibits a step change, the power output of the TEG does not change correspondingly and there is a significant response delay, as shown in Fig. 8(a). The power output at the intersection of power curves between T_{ex} step increase and T_{ex} step decrease is exactly equal to the average value under steady-state conditions, because the power output is directly proportional to exhaust temperature. However, the output power at the intersection of $\dot{m}_{ex}$ power curves is lower than the steady-state average value. This can be attributed to the fact that, within a certain range of relatively high mass flow rates, the output power exhibits only slight variations in response to changes in the mass flow rate. As a result, even at the maximum mass flow rate of 50 g/s, the generated output power is only marginally higher than that observed at the steady-state value of 30 g/s. Unlike the power output, the exhaust outlet temperature exhibits step change trends consistent with the exhaust heat, as shown in Fig. 8(b), because most of the heat is directly discharged with the exhaust gas, and only a small portion is converted into electrical energy by the TEG. Additionally, Figs 3(a) and (d) and Fig. 8(a) clearly demonstrate the presence of a substantial response hysteresis during the heat-to-electricity conversion process.

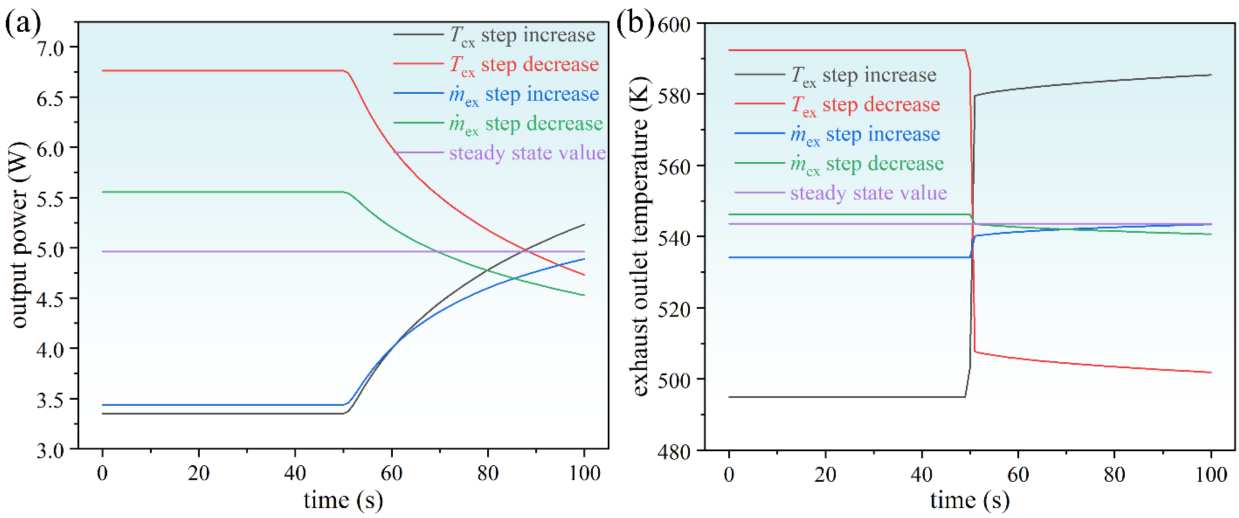

Fig. 8. Output power and exhaust outlet temperature of the TEG under step increase and decrease of the exhaust heat. (a) Output power; (b) Exhaust outlet temperature.

Fig. 9 illustrates the dynamic conversion efficiency and heat absorption of the TEG under step increase and decrease of the exhaust heat. Here, the curve part with negative efficiency and heat absorption is not given, as it is meaningless. Unlike the output power, conversion efficiency fluctuates sharply with the change of exhaust heat, as shown in Fig. 9(a). In the case of step changes in exhaust mass flow rate, the conversion efficiency exhibits inverse variations, being inversely proportional to the mass flow rate. Consequently, a step decrease in exhaust mass flow rate can significantly enhance the conversion efficiency. As for step changes of exhaust temperature, when the exhaust temperature step decreases, the conversion efficiency becomes negative, because the exhaust outlet temperature is already higher than the exhaust inlet temperature, and in this case, the instantaneous heat absorption is negative, as shown in Fig. 9(b). However, the negative value of conversion efficiency does not make sense, and it is not reasonable to use instantaneous conversion efficiency to examine the behavior of the TEG. Instead, the mean conversion efficiency over a period of time should be used.

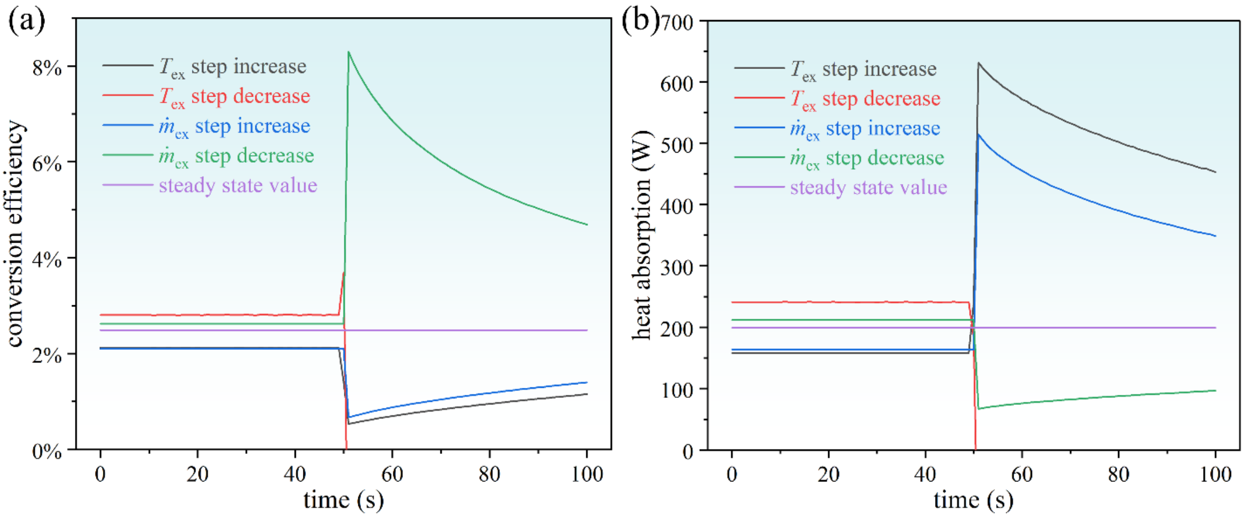

Fig. 9. Conversion efficiency and heat absorption of the TEG under step increase and decrease of the exhaust heat. (a) Conversion efficiency; (b) Heat absorption.

4.3 Dynamic characteristics under linear increase and decrease of the exhaust heat

In most cases, the exhaust heat does not show a step change, but rather a linear change. Fig. 10 gives the dynamic output power and exhaust outlet temperature of the TEG under linear increase and decrease of the exhaust heat, where the exhaust heat changes from t = 10 s to t = 90 s. Similarly, the mean output power of both linear increase and linear decrease in $\dot{m}_{ex}$ is lower than the steady-state average output power, while the mean output power of linear changes in T_{ex} is equal to the steady-state average value, as can be observed in Fig. 10(a). The corresponding reasons in Fig. 8(a) can explain this phenomenon. As depicted in Fig. 10(b), the exhaust outlet temperature is predominantly determined by the exhaust inlet temperature, with only a minor influence from the exhaust mass flow rate. It seems that the fluctuation of exhaust temperature has a greater influence on the dynamic characteristics of the TEG than the fluctuation of exhaust mass flow rate.

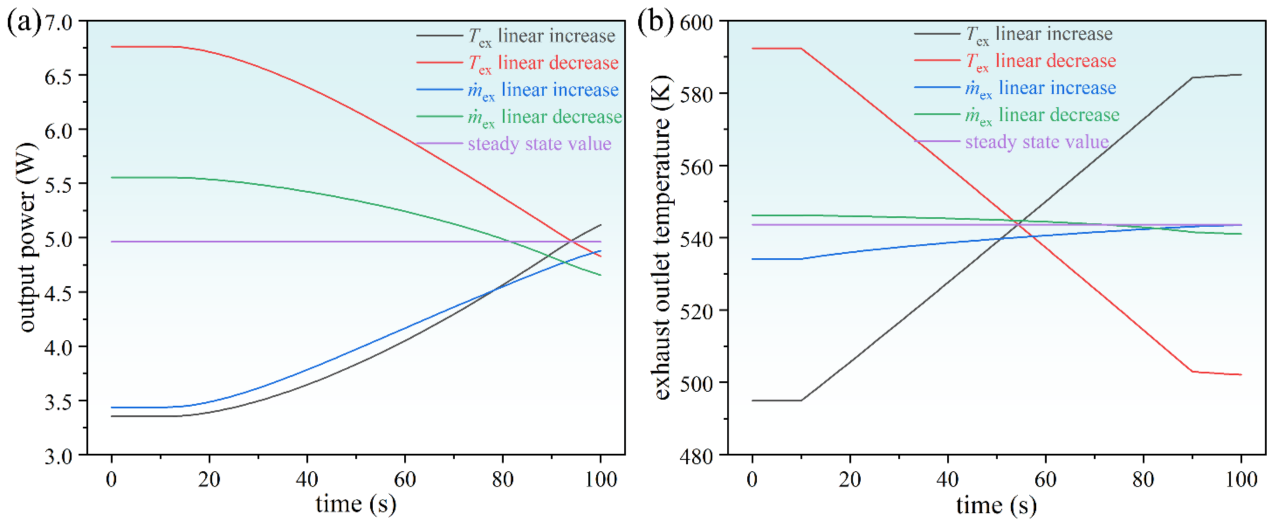

Fig. 10. Output power and exhaust outlet temperature of the TEG under linear increase and decrease of the exhaust heat. (a) Output power; (b) Exhaust outlet temperature.

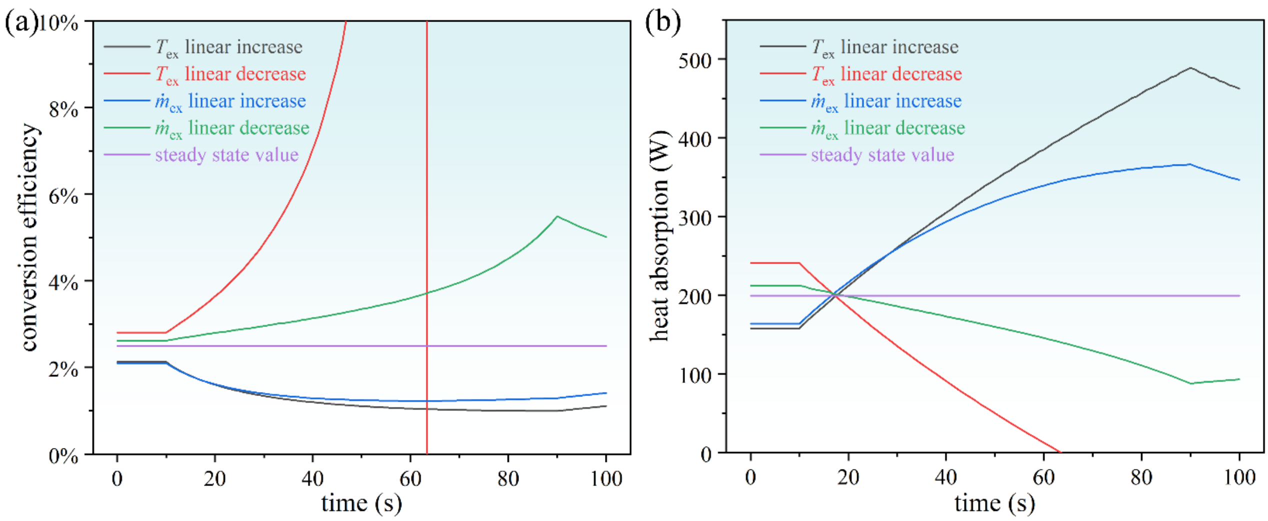

Fig. 11. Conversion efficiency and heat absorption of the TEG under linea increase and decrease of the exhaust heat. (a) Conversion efficiency; (b) Heat absorption.

Fig. 11 illustrates the dynamic conversion efficiency and heat absorption of the TEG under linear increase and decrease of the exhaust heat. The linear increase both in T_{ex} and $\dot{m}_{ex}$ may deteriorate the conversion efficiency, as shown in Fig. 11(a). Although the increase in exhaust heat can amplify the power output of the TEG, the heat absorption also increases, and the increase in heat absorption is greater than the increase in power (as shown in Fig. 11(b)), resulting in a decrease in conversion efficiency. Also, in the case of a rapid increase in exhaust heat, due to the influence of thermal inertia, the hot-side temperature of the TEM presents a slow increase, so that the power output will not immediately respond to the change of exhaust heat. By taking the average of the dynamic conversion efficiency during both linear decrease and linear increase in mass flow rate, it is found to be higher than the conversion efficiency under steady-state conditions. This indicates that even when the mass flow fluctuates between linear increase and decrease, the conversion efficiency of the TEG can be significantly improved. The subsequent section explores the impact of periodic changes in exhaust heat on the output performance of the TEG.

4.4 Dynamic characteristics under triangular and sine waves of the exhaust heat

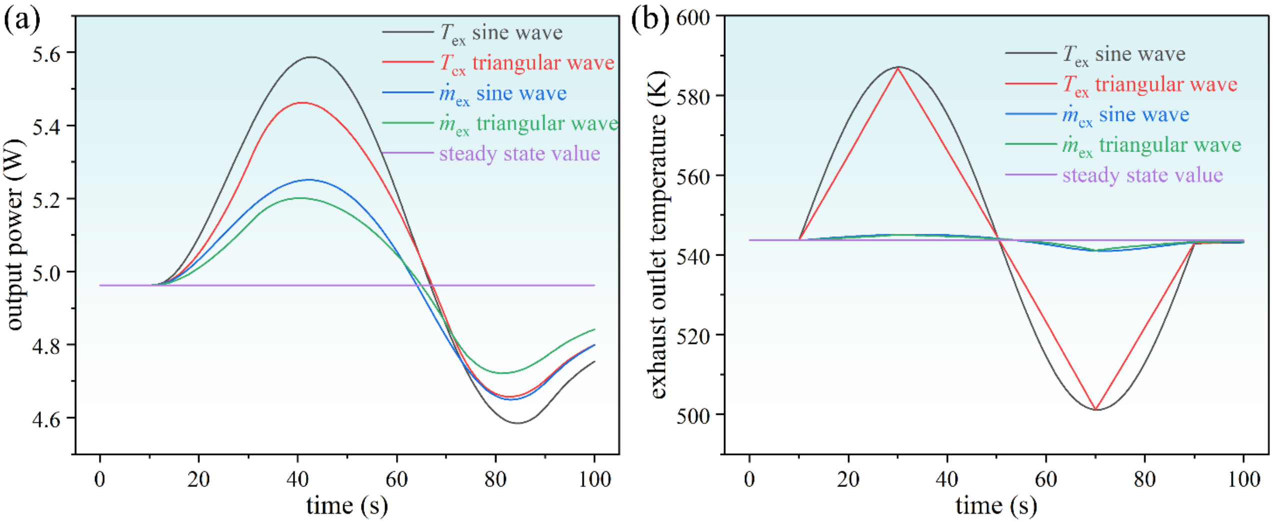

Fig. 12. Output power and exhaust outlet temperature of the TEG under triangular and sine waves of the exhaust heat. (a) Output power; (b) Exhaust outlet temperature.

In practical applications, exhaust heat may exhibit periodic changes, for example, during the repeated switching process of vehicle acceleration and deceleration, the automobile exhaust heat may fluctuate repeatedly between a maximum and a minimum value. In this section, two typical periodic exhaust heat sources, triangular and sine waves, are used as the research objectives. Fig. 12(a) shows the dynamic output power of the TEG under triangular and sine waves of the exhaust heat. In the case of triangular waves, the changing amplitude of output power under triangular waves is smaller than that of sine waves, and the output power exhibits a sine wave variation, which can be attributed to thermal inertia. Thermal inertia acts as a buffer and filter during the heat transfer from exhaust heat to the hot side of the TEM. Besides, it is observed that the mean output power under T_{ex} triangular and sine waves may be higher than the steady-state power. Fig. 12(b) shows the dynamic exhaust outlet temperature under triangular and sine waves of the exhaust heat. Similarly, since the exhaust outlet temperature is mainly influenced by its inlet temperature, the curves under T_{ex} sine and triangular waves are completely consistent with the inlet temperature curves in Fig. 3(c).

Fig. 13(a) gives the dynamic conversion efficiency of the TEG under triangular and sine waves of the exhaust heat. The conversion efficiency under T_{ex} triangular and sine waves exhibits irregular changes due to the negative value or values close to 0 K of temperature difference from the exhaust inlet to the exhaust outlet, as can be found from the heat absorption in Fig. 13(b). In practice, when the exhaust mass flow rate is kept constant, the exhaust temperature shows a gradual and continuous change without the periodic fluctuations illustrated in Figs 3(a)-(c). Consequently, the dynamic conversion efficiency under fluctuations of exhaust temperature does not have practical significance, and the key purpose of this work is to compare which parameter, exhaust temperature or mass flow rate, has a greater impact on the dynamic characteristics of the TEG. On the contrary, exhaust mass flow rate with any waveform exists in actual situations. The results demonstrate that the average conversion efficiency during triangular and sine wave fluctuations in exhaust mass flow rate is higher compared to the steady-state value. When considering Fig. 12(a), it can be inferred that while the periodic fluctuation of exhaust mass flow rate does not significantly enhance the output power, it does effectively improve the conversion efficiency.

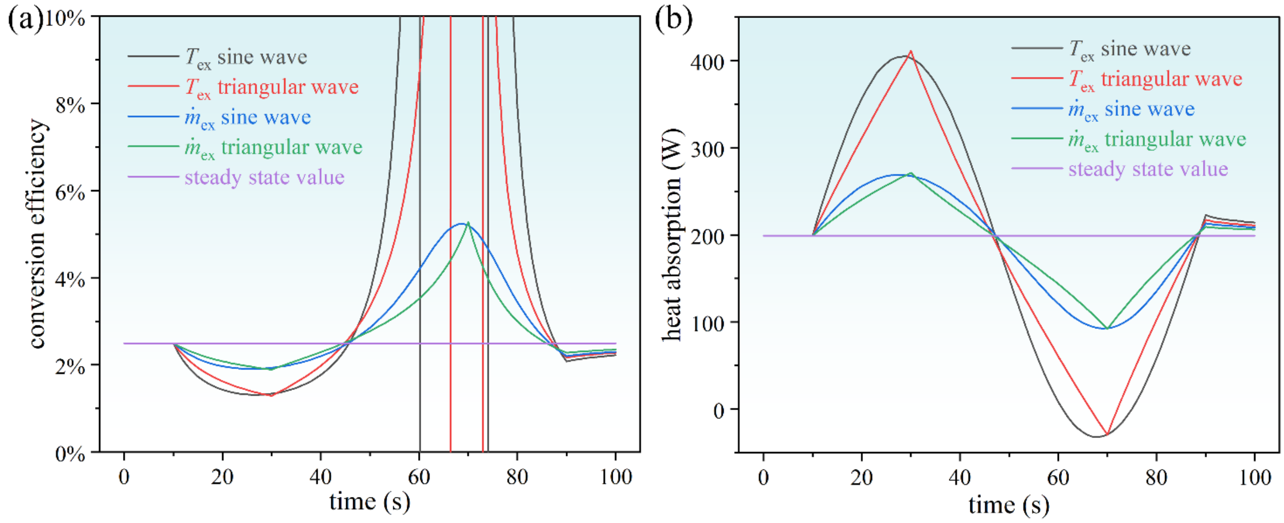

Fig. 13. Conversion efficiency and heat absorption of the TEG under triangular and sine waves of the exhaust heat. (a) Conversion efficiency; (b) Heat absorption.

4.5 Comparison of output performance under different fluctuations of the exhaust heat

Fig. 14 illustrates a comparison of output performance under different fluctuations of the exhaust heat, where the dotted line represents the steady-state value. It is obvious that the step and linear decreases of exhaust heat can amplify the output power and conversion efficiency, whereas the step and linear increases of exhaust heat may deteriorate the dynamic performance. Compared to the steady power of 4.96 W and efficiency of 2.49%, the TEG demonstrates an increase in mean output power and conversion efficiency of 5.50% and 70.61%, and 6.04% and 45.05% respectively, when the exhaust mass flow rate is decreased in step and linear trends. However, in practical applications, the fluctuation of exhaust heat can not always maintain a downward trend, but is accompanied by an upward trend. Hence, examining the impact of periodic exhaust heat considering both upward and downward trends is more relevant to real-world scenarios. The dynamic output power of the TEG is found to increase by 2.09% and 1.61% under sine and triangular waves of exhaust temperature, respectively, compared to the steady-state power. Furthermore, when subjected to sine and triangular waves of exhaust mass flow rate, the mean output power of the TEG shows a slight increase, while the mean conversion efficiency significantly improves by 15.58% and 10.14% respectively. These results demonstrate that periodic exhaust heat can effectively enhance the dynamic output performance of the TEG, especially in terms of conversion efficiency. Additionally, the fluctuation of exhaust temperature has a stronger impact on the dynamic characteristics of the TEG than the fluctuation of exhaust mass flow rate.

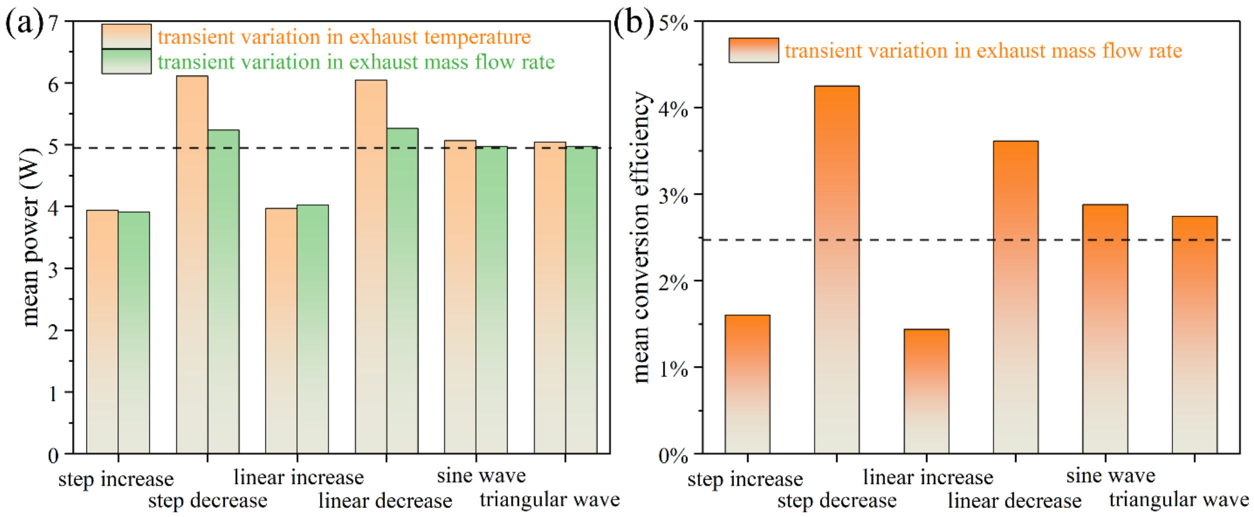

Fig. 14. Comparison of output performance under different fluctuations of the exhaust heat. (a) Mean power; (b) Mean conversion efficiency.

5. Conclusions

In the field of waste heat recovery, thermoelectric generators display notable dynamic characteristics when exposed to fluctuations in exhaust heat. This study utilizes a transient fluid-thermal-electric multiphysics model to evaluate the dynamic output performance of the thermoelectric generator under six fundamental waveforms of exhaust heat, including step increase and decrease, linear increase and decrease, as well as triangular and sine waves. By analyzing the transient simulation results, a comprehensive understanding of the thermoelectric generator's dynamic behavior is achieved, allowing for an in-depth assessment of its dynamic output power and conversion efficiency across varying exhaust heat fluctuations. Furthermore, a comparison is made with the steady-state output performance to provide insights into the thermoelectric generator's behavior in dynamic operating conditions. The key findings are summarized as follows:

(1) To ensure high reasonability and accuracy of numerical simulations, it is necessary to consider the impedance matching characteristics of the electric field, and the hot-side temperature of the thermoelectric module decreases with the decrease in load resistance due to the Peltier effect.

(2) The downward trends in exhaust heat are beneficial for improving the dynamic performance of the TEG. Specifically, when the exhaust mass flow rate step decreases, compared with the steady power and efficiency of 4.96 W and 2.49%, the mean output power and conversion efficiency increase by 5.50% and 70.61%, respectively, while when in a linear decrease, they increase by 6.04% and 45.05%, respectively. However, the upward trends in exhaust heat may lower the dynamic performance of the TEG.

(3) Fluctuations in exhaust temperature have a more pronounced effect on the dynamic characteristics of the TEG than fluctuations in exhaust mass flow rate. Besides, implementing periodic variations in exhaust heat can effectively enhance power and efficiency, specifically conversion efficiency, and smoother changes can lead to superior performance. When subjected to a sin wave of exhaust mass flow rate, the conversion efficiency experiences a 15.58% improvement.

(4) In practical applications, exhaust temperature and mass flow rate are interconnected, and temperature variations commonly accompany changes in mass flow rate. Therefore, future investigations will focus on exploring the combined effects of both simultaneous variations on the dynamic characteristics of the TEG.

Acknowledgments

This work was supported by the National Natural Science Foundation of China (Grant Nos. 52306017, U20A20301, 52250273) and the Natural Science Foundation of Hubei Province (No. 2023AFB093).

References

[1] Gonca G, Sahin B, Parlak A, Ayhan V, Cesur İ, Koksal S. Application of the Miller cycle and turbo charging into a diesel engine to improve performance and decrease NO emissions. Energy. 2015;93:795-800.

[2] Laux C, Gotter A, Eckert F, Neef M. Experimental results of a low-pressure steam Rankine cycle with a novel water lubricated radial inflow turbine for the waste heat utilization of internal combustion engines. Energy Convers Manage 2022;271:116265.

[3] Vannoni A, Sorce A, Traverso A, Fausto Massardo A. Techno-economic optimization of high-temperature heat pumps for waste heat recovery. Energy Convers Manage 2023;290:117194.

[4] Shen Z-G, Tian L-L, Liu X. Automotive exhaust thermoelectric generators: Current status, challenges and future prospects. Energy Convers Manage 2019;195:1138-73.

[5] Massaguer A, Pujol T, Comamala M, Massaguer E. Feasibility study on a vehicular thermoelectric generator coupled to an exhaust gas heater to improve aftertreatment's efficiency in cold-starts. Appl Therm Eng 2020;167:114702.

[6] Yazawa K, Shakouri A. Fuel-burning thermoelectric generators for the future of electric vehicles. Energy Convers Manage 2021;227:113523.

[7] Luo D, Sun Z, Wang R. Performance investigation of a thermoelectric generator system applied in automobile exhaust waste heat recovery. Energy. 2022;238:121816.

[8] Miao Z, Meng X, Liu L. Improving the ability of thermoelectric generators to absorb industrial waste heat through three-dimensional structure optimization. Appl Therm Eng 2023;228:120480.

[9] Wang C, Tang S, Liu X, Su GH, Tian W, Qiu S. Experimental study on heat pipe thermoelectric generator for industrial high temperature waste heat recovery. Appl Therm Eng 2020;175:115299.

[10] Nour Eddine A, Chalet D, Faure X, Aixala L, Chessé P. Optimization and characterization of a thermoelectric generator prototype for marine engine application. Energy. 2018;143:682-95.

[11] Georgopoulou CA, Dimopoulos GG, Kakalis NMP. A modular dynamic mathematical model of thermoelectric elements for marine applications. Energy. 2016;94:13-28.

[12] Quan R, Liang W, Quan S, Huang Z, Liu Z, Chang Y, et al. Performance interaction assessment of automobile exhaust thermoelectric generator and engine under different operating conditions. Appl Therm Eng 2022;216:119055.

[13] Lan S, Stobart R, Chen R. Performance comparison of a thermoelectric generator applied in conventional vehicles and extended-range electric vehicles. Energy Convers Manage 2022;266:115791.

[14] Luo D, Wu Z, Yan Y, Ji D, Cheng Z, Wang R, et al. Optimal design of a heat exchanger for automotive thermoelectric generator systems applied to a passenger car. Appl Therm Eng 2023;227:120360.

[15] Frobenius F, Gaiser G, Rusche U, Weller B. Thermoelectric Generators for the Integration into

Automotive Exhaust Systems for Passenger Cars and Commercial Vehicles. J Electron Mater 2016;45:1433-40.
[16] Crane D, LaGrandeur J, Jovovic V, Ranalli M, Adldinger M, Poliquin E, et al. TEG On-Vehicle Performance and Model Validation and What It Means for Further TEG Development. J Electron Mater 2013;42:1582-91.
[17] Chen W-H, Lin Y-X, Chiou Y-B, Lin Y-L, Wang X-D. A computational fluid dynamics (CFD) approach of thermoelectric generator (TEG) for power generation. Appl Therm Eng 2020;173:115203.
[18] Luo D, Wang R, Yu W, Sun Z, Meng X. Modelling and simulation study of a converging thermoelectric generator for engine waste heat recovery. Appl Therm Eng 2019;153:837-47.
[19] Luo D, Wang R, Yu W, Zhou W. A numerical study on the performance of a converging thermoelectric generator system used for waste heat recovery. Appl Energy 2020;270:115181.
[20] Chen W-H, Chiou Y-B, Chein R-Y, Uan J-Y, Wang X-D. Power generation of thermoelectric generator with plate fins for recovering low-temperature waste heat. Appl Energy 2022;306:118012.
[21] Zhao Y, Lu M, Li Y, Wang Y, Ge M. Numerical investigation of an exhaust thermoelectric generator with a perforated plate. Energy. 2023;263:125776.
[22] Cai H, Ye Z, Liu G, Romagnoli A, Ji D. Sizing optimization of thermoelectric generator for low-grade thermal energy utilization: Module level and system level. Appl Therm Eng 2023;221:119823.
[23] Catalan L, Araiz M, Aranguren P, Astrain D. Computational study of geothermal thermoelectric generators with phase change heat exchangers. Energy Convers Manage 2020;221:113120.
[24] Yan S-R, Moria H, Asaadi S, Sadighi Dizaji H, Khalilarya S, Jermsittiparsert K. Performance and profit analysis of thermoelectric power generators mounted on channels with different cross-sectional shapes. Appl Therm Eng 2020:115455.
[25] Luo D, Wu Z, Yan Y, Cao J, Yang X, Zhao Y, et al. Performance investigation and design optimization of a battery thermal management system with thermoelectric coolers and phase change materials. Journal of Cleaner Production. 2024;434:139834.
[26] Li B, Huang K, Yan Y, Li Y, Twaha S, Zhu J. Heat transfer enhancement of a modularised thermoelectric power generator for passenger vehicles. Appl Energy 2017;205:868-79.
[27] Luo D, Liu Z, Yan Y, Li Y, Wang R, Zhang L, et al. Recent advances in modeling and simulation of thermoelectric power generation. Energy Convers Manage 2022;273:116389.

[28] Massaguer A, Massaguer E, Comamala M, Pujol T, Montoro L, Cardenas MD, et al. Transient behavior under a normalized driving cycle of an automotive thermoelectric generator. Appl Energy 2017;206:1282-96.

[29] Lan S, Yang Z, Chen R, Stobart R. A dynamic model for thermoelectric generator applied to vehicle waste heat recovery. Appl Energy 2018;210:327-38.

[30] Luo D, Yan Y, Chen W-H, Yang X, Chen H, Cao B, et al. A comprehensive hybrid transient CFD-thermal resistance model for automobile thermoelectric generators. Int J Heat Mass Transfer 2023;211:124203.

[31] Yan Y, Malen JA. Periodic heating amplifies the efficiency of thermoelectric energy conversion. Energy Environ Sci 2013;6:1267-73.

[32] Luo D, Wang R, Yu W, Zhou W. A novel optimization method for thermoelectric module used in waste heat recovery. Energy Convers Manage 2020;209:112645.

[33] Luo D, Yan Y, Li Y, Yang X, Chen H. Exhaust channel optimization of the automobile thermoelectric generator to produce the highest net power. Energy. 2023;281:128319.

[34] Zhang Q, Liao J, Tang Y, Gu M, Ming C, Qiu P, et al. Realizing a thermoelectric conversion efficiency of 12% in bismuth telluride/skutterudite segmented modules through full-parameter optimization and energy-loss minimized integration. Energy Environ Sci 2017;10:956-63.

[35] Luo D, Li Y, Yan Y, Hu X, Fan Xa, Chen W-H, et al. Realizing ultrahigh ZT value and efficiency of the Bi2Te3 thermoelectric module by periodic heating. Energy Convers Manage 2023;296:117669.

[36] Luo D, Wang R, Yan Y, Yu W, Zhou W. Transient numerical modelling of a thermoelectric generator system used for automotive exhaust waste heat recovery. Appl Energy 2021;297:117151.